Chapter 4
Optical Fiber Gratings for Mechanical and Bio-sensing

Young-Geun Han

4.1 Theoretical Analysis of Fiber Gratings

In general, optical fiber gratings can be classified as either fiber Bragg gratings (FBGs) or long-period fiber gratings (LPGs) depending on whether the periodic variation in the refractive index is ranged in the submicron or in the hundreds of microns scale [1, 2]. Figure 4.1 shows the operating principle of FBGs and LPGs. The periodic modulation in the refractive index induce, in the case of FBGs, mode coupling between two counter-propagating modes, whereas in the case of LPGs, it causes coupling between core and cladding modes. FBGs can be used to perform a wide range of functions, such as reflection, filtering, and sensing. Depending on the configuration of their physical structures such as index profile, grating period and tilt, FBGs can be categorized as either uniform FBGs, apodized FBGs, blazed FBGs, or chirped FBGs. Theoretical analysis of fiber gratings can be readily obtained by solving Maxwell's equation and considering small index perturbation [3–5].

In order to analyze optical characteristics of LPGs and FBGs, let's drive the coupled mode equation starting from Maxwell's equation. Assume that each field can be decomposed into spatial and temporal terms as:

$$\begin{aligned} \vec{E} &= \vec{E}(\vec{r},t) = \vec{E}(\vec{r})e^{-i\omega t} \\ \vec{H} &= \vec{H}(\vec{r},t) = \vec{H}(\vec{r})e^{-i\omega t} \end{aligned} \tag{4.1}$$

Assuming that the medium is linear, homogeneous and isotropic, ε μ, σ are independent of $\vec{H}$, $\vec{E}$, space or time and direction, the Maxwell's equation for a monochromatic wave can be written as:

Y.-G. Han (✉)
Department of Physics, Hanyang University, 17 Haengdang-dong, Seongdong-gu, Seoul 133-791, Korea
e-mail: yghan@hanyang.ac.kr

J. U. Kang (ed.), *Fiber Optic Sensing and Imaging*,
DOI: 10.1007/978-1-4614-7482-1_4,

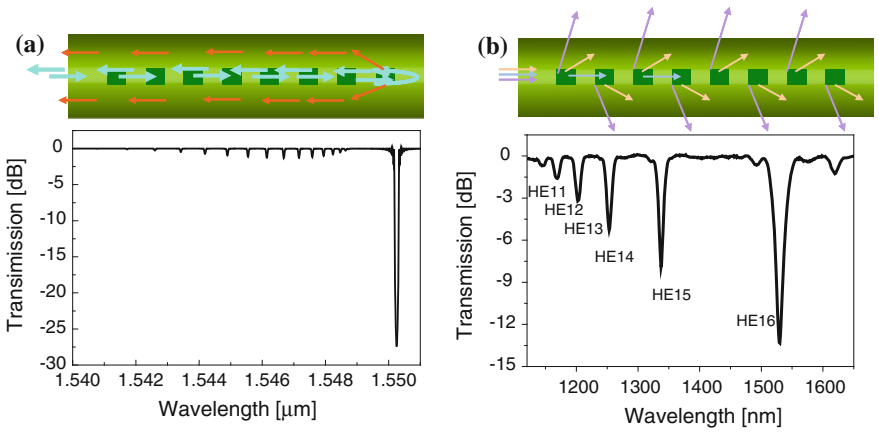

Fig. 4.1 Operating principle of (**a**) fiber Bragg gratings and (**b**) long-period fiber gratings

$$\begin{aligned} \nabla \times \vec{H}(\vec{r}) &= -i\omega\varepsilon\vec{E}(\vec{r}) \\ \nabla \times \vec{E}(\vec{r}) &= i\omega\mu\vec{H}(\vec{r}) \end{aligned} \tag{4.2}$$

$$\begin{aligned} \nabla \times \vec{H}(\vec{r}) &= -i\omega\varepsilon\vec{E}(\vec{r}) \\ \nabla \times \vec{E}(\vec{r}) &= i\omega\mu\vec{H}(\vec{r}) \end{aligned} \tag{4.3}$$

Assuming that the wave propagates in z-direction, and the special term of fields can be decomposed into transverse and longitudinal components as

$$\begin{aligned} \vec{E}(\vec{r}) &= \vec{E}_t(\vec{r}) + \vec{E}_z(\vec{r}) \\ \vec{H}(\vec{r}) &= \vec{H}_t(\vec{r}) + \vec{H}_z(\vec{r}) \end{aligned} \tag{4.4}$$

Then the Maxwell's equation can be decomposed into transverse and longitudinal components.

Transverse components:

$$\begin{aligned} \nabla_t \times \vec{H}_z(\vec{r}) + \nabla_z \times \vec{H}_t(\vec{r}) &= -i\omega\varepsilon\vec{E}_t(\vec{r}) \\ \nabla_t \times \vec{E}_z(\vec{r}) + \nabla_z \times \vec{E}_t(\vec{r}) &= i\omega\mu\vec{H}_t(\vec{r}) \end{aligned} \tag{4.5}$$

Longitudinal components:

$$\begin{aligned} \nabla_t \times \vec{H}_t(\vec{r}) &= -i\omega\varepsilon\vec{E}_z(\vec{r}) \\ \nabla_t \times \vec{E}_t(\vec{r}) &= i\omega\mu\vec{H}_z(\vec{r}) \end{aligned} \tag{4.6}$$

The transverse mode equation can be obtained by applying $\hat{e}_z\times$ on Eq. (4.5) which results in:

$$\begin{aligned}\frac{\partial \vec{H}_z(\vec{r})}{\partial z} - i\omega\varepsilon\hat{e}_z \times \vec{E}_t(\vec{r}) &= \nabla_t \vec{H}_z(\vec{r}) \\ \frac{\partial \vec{E}_z(\vec{r})}{\partial z} + i\omega\mu\hat{e}_z \times \vec{H}_t(\vec{r}) &= \nabla_t \vec{E}_z(\vec{r})\end{aligned} \tag{4.7}$$

The longitudinal mode equations from Eq. (4.6) can be obtained as

$$\begin{aligned}\vec{E}_z(\vec{r}) &= \tfrac{i}{\omega\varepsilon}\nabla_t \times \vec{H}_t(\vec{r}) \\ \vec{H}_z(\vec{r}) &= \tfrac{-i}{\omega\mu}\nabla_t \times \vec{E}_t(\vec{r})\end{aligned} \tag{4.8}$$

By substituting Eq. (4.8) into Eq. (4.5), the transverse mode equation can be expressed by

$$\begin{aligned}\nabla_t \times \frac{-i}{\omega\mu}\nabla_t \times \vec{E}_t(\vec{r}) + \nabla_z \times \vec{H}_t(\vec{r}) &= -i\omega\varepsilon\vec{E}_t(\vec{r}) \\ \nabla_t \times \frac{i}{\omega\varepsilon}\nabla_t \times \vec{H}_t(\vec{r}) + \nabla_z \times \vec{E}_t(\vec{r}) &= i\omega\mu\vec{H}_t(\vec{r})\end{aligned} \tag{4.9}$$

For an ideal waveguide, the mode profile can be written as:

$$\begin{aligned}\vec{E}(\vec{r},t) &= \vec{E}_l(x,y)e^{i\beta_l z - i\omega t} \\ \vec{H}(\vec{r},t) &= \vec{H}_l(x,y)e^{i\beta_l z - i\omega t},\end{aligned} \tag{4.10}$$

where β_l is the propagating constant of the lth order mode.

Since $\mu = \mu_0, \varepsilon = \varepsilon_0 n_0^2(x,y)$, where n_0 is a refractive index in an ideal waveguide, then, Eq. (4.5) in the ideal mode case can be modified as:

$$\begin{aligned}\frac{-i}{\omega\mu_0}\nabla_t \times \nabla_t \times \vec{E}_{l,t}(x,y) + i\beta_l\hat{e}_z \times \vec{H}_{l,t}(\vec{r}) &= -i\omega\varepsilon_0 n_0^2(x,y)\vec{E}_{l,t}(x,y) \\ \frac{i}{\omega\varepsilon_0}\nabla_t \times \left(\frac{1}{n_0^2(x,y)}\nabla_t \times \vec{H}_{l,t}(\vec{r})\right) + i\beta_l\hat{e}_z \times \vec{E}_{l,t}(\vec{r}) &= i\omega\mu_0\vec{H}_{l,t}(\vec{r})\end{aligned} \tag{4.11}$$

where $\vec{E}_{l,t}$ and $\vec{H}_{l,t}$ are the transverse field of the lth order ideal mode for electric and magnetic waves in an ideal waveguide. β_l is the propagating constant of the lth order mode.

For the perturbed waveguide, we can expand the perturbed field with a linear summation of ideal normal modes such as:

$$\begin{aligned}\vec{E}_t(\vec{r}) &= \sum_{l=0}^{\infty} c_l e^{i\beta_l z}\vec{E}_{l,t}(x,y) = \sum_{l=0}^{\infty} a_l(z)\vec{E}_{l,t}(x,y) \\ \vec{H}_t(\vec{r}) &= \sum_{l=0}^{\infty} g_l e^{i\beta_l z}\vec{H}_{l,t}(x,y) = \sum_{l=0}^{\infty} b_l(z)\vec{H}_{l,t}(x,y)\end{aligned} \tag{4.12}$$

where the constant c_l and g_l are the slowly varying modal amplitudes that include phase term for electric and magnetic waves, respectively. $a_l(z)$ and $b_l(z)$ are the rapidly varying modal amplitudes that include phase term for electric and magnetic waves, respectively. Since $\mu = \mu_0, \varepsilon = \varepsilon_0 n^2(\vec{r})$, Eq. (4.9) can be modified by

inserting Eq. (4.12) into Eq. (4.9). From that we obtain the governing equations for the perturbed waveguide as:

$$\frac{-i}{\omega\mu_0}\sum a_l(z)\nabla_t\times\nabla_t\times\vec{E}_{l,t}(x,y)+\sum_{l=0}^{\infty}\frac{\partial b_l(z)}{\partial z}\hat{e}_z\times\vec{H}_{l,t}(x,y)=-i\omega\varepsilon_0 n^2(\vec{r})\sum_{l=0}^{\infty}a_l(z)\vec{E}_{l,t}(x,y)$$

$$\frac{i}{\omega\varepsilon_0}\sum b_l(z)\nabla_t\times\left(\frac{i}{n_0^2(\vec{r})}\nabla_t\times\vec{H}_{l,t}(x,y)\right)+\sum_{l=0}^{\infty}\frac{\partial a_l(z)}{\partial z}\hat{e}_z\times\vec{E}_t(\vec{r})=i\omega\mu_0\sum_{l=0}^{\infty}b_l(z)\vec{H}_{l,t}(x,y) \tag{4.13}$$

By substituting appropriate equations in the ideal waveguide into Eq. (4.13), we have

$$\begin{aligned}&\sum a_l(z)\left(-i\beta_l\hat{e}_z\times\vec{H}_{l,t}(x,y)-i\omega\varepsilon_0 n_0^2(x,y)\vec{E}_{l,t}(x,y)\right)\vec{E}_{l,t}(x,y)+\sum_{l=0}^{\infty}\frac{\partial b_l(z)}{\partial z}\hat{e}_z\times\vec{H}_{l,t}(x,y)\\&=-i\omega\varepsilon_0 n^2(\vec{r})\sum_{l=0}^{\infty}a_l(z)\vec{E}_{l,t}(x,y)\\&\frac{i}{\omega\varepsilon_0}\sum b_l(z)\nabla_t\times\left(\left(\frac{i}{n_0^2(x,y)}-\frac{i}{n^2(\vec{r})}\right)\nabla_t\times\vec{H}_{l,t}(x,y)\right)+\sum_{l=0}^{\infty}\left(i\beta_l b_l(z)-\frac{\partial a_l(z)}{\partial z}\right)\hat{e}_z\times\vec{E}_t(\vec{r})=0\end{aligned} \tag{4.14}$$

Rearranging Eq. (4.14) results in:

$$\begin{aligned}&\sum_{l=0}^{\infty}\left(\frac{\partial b_l(z)}{\partial z}-i\beta_l a(z)\right)\hat{e}_z\times\vec{H}_{l,t}(x,y)+i\omega\varepsilon_0\left(n^2(\vec{r})-n_0^2(x,y)a_l(z)\right)\vec{E}_{l,t}(x,y)=0\\&\sum_{l=0}^{\infty}\left(i\beta_l b_l(z)-\frac{\partial a_l(z)}{\partial z}\right)\hat{e}_z\times\vec{E}_t(\vec{r})+\tfrac{i}{\omega\varepsilon_0}\sum b_l(z)\nabla_t\times\left(\left(\frac{i}{n_0^2(x,y)}-\frac{i}{n^2(\vec{r})}\right)\nabla_t\times\vec{H}_{l,t}(x,y)\right)=0\end{aligned} \tag{4.15}$$

Using the equations for normal modes and using the normalization and orthogonalization conditions such as,

$$\int\hat{e}_z\cdot(\vec{E}_{m,t}(x,y)\times\vec{H}^*_{l,t}(x,y))dA=2\frac{\beta_l^*}{|\beta_l|}P\delta_{m,l}, \tag{4.16}$$

Where $\delta_{m,l}=1$ for $m=l$ and $\delta_{m,l}=0$ for $m\neq l$

Equation (4.15) can be modified by multiplying the terms with either $\int\vec{E}_{m,t}(x,y)\cdot$ or $\int\vec{H}_{m,t}(x,y)\cdot$

$$\begin{aligned}&\int\vec{E}_{m,t}(x,y)\cdot\left(\sum_{l=0}^{\infty}\left(\frac{\partial b_l(z)}{\partial z}-i\beta_l a(z)\right)\hat{e}_z\times\vec{H}_{l,t}(x,y)+i\omega\varepsilon_0\left(n^2(\vec{r})-n_0^2(x,y)a_l(z)\right)\vec{E}_{l,t}(x,y)=0\right)\\&\int\vec{H}_{m,t}(x,y)\cdot\left(\sum_{l=0}^{\infty}\left(\frac{\partial a_l(z)}{\partial z}-i\beta_l b_l(z)\right)\hat{e}_z\times\vec{E}_{l,t}(\vec{r})+\tfrac{i}{\omega\varepsilon_0}\sum b_l(z)\nabla_t\times\left(\left(\tfrac{i}{n^2(\vec{r})}-\tfrac{i}{n_0^2(x,y)}\right)\nabla_t\times\vec{H}_{l,t}(x,y)\right)=0\right)\end{aligned} \tag{4.17}$$

Then Eq. (4.17) can be modified by using Eq. (4.16)

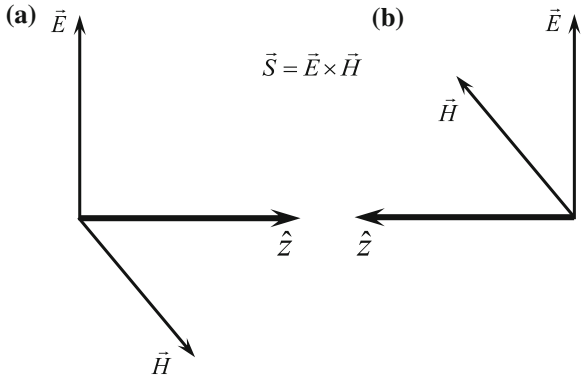

Fig. 4.2 Direction of pointing vector ($\vec{S} = \vec{E} \times \vec{H}$) propagating (**a**) forward z-direction or (**b**) backward -z-direction

$$\begin{aligned} \frac{\partial b_m(z)}{\partial z} - i\beta_m a(z) &= 2\sum_{l=0}^{\infty} a_l(z) K_{m,l}(z) \\ \frac{\partial a_m(z)}{\partial z} - i\beta_m b_m(z) &= 2\sum_{l=0}^{\infty} b_l(z) C_{m,l}(z) \end{aligned} \tag{4.18}$$

Where

$$\begin{aligned} K_{m,l}(z) &= \frac{i\omega\varepsilon_0}{4P}\frac{|\beta_m|}{\beta_m}\int \left(n^2(\vec{r}) - n_0^2(x,y)\right)\vec{E}^*_{m,t}(x,y)\cdot\vec{E}_{l,t}(x,y)dA \\ C_{m,l}(z) &= \frac{i\omega\varepsilon_0}{4P}\frac{|\beta_m|}{\beta_m^*}\int \frac{n_0^2(x,y)}{n^2(\vec{r})}\left(n^2(\vec{r}) - n_0^2(x,y)\right)\vec{E}^*_{m,z}(x,y)\cdot\vec{E}_{l,z}(x,y)dA \end{aligned} \tag{4.19}$$

The solutions for the mode coupling can be expressed as:

$$\begin{aligned} a_m(z) &= a_m^{(+)}(z) + a_m^{(-)}(z) = c_m^{(+)}(z)e^{i\beta_m z} + c_m^{(-)}(z)e^{-i\beta_m z} \\ b_m(z) &= a_m^{(+)}(z) - a_m^{(-)}(z) = c_m^{(+)}(z)e^{i\beta_m z} - c_m^{(-)}(z)e^{-i\beta_m z} \end{aligned} \tag{4.20}$$

Where $c_m^{(\pm)}$ is the amplitude for the waves propagating in forward (+) or or backward (−) direction. Here, it is evident that the relative direction of the magnetic field over the electric field of a mode is reversed when the propagation direction is reversed in an ideal waveguide as seen in Fig. 4.2.

By substituting Eq. (4.20) into Eq. (4.18), we obtain

$$\begin{aligned} \frac{\partial}{\partial z}\left(a_m^{(+)}(z) + a_m^{(-)}(z)\right) - i\beta_m\left(a_m^{(+)}(z) + a_m^{(-)}(z)\right) &= 2\sum_{l=0}^{\infty}\left(a_l^{(+)}(z) + a_l^{(-)}(z)\right)K_{m,l}(z) \\ \frac{\partial}{\partial z}\left(a_m^{(+)}(z) - a_m^{(-)}(z)\right) - i\beta_m\left(a_m^{(+)}(z) - a_m^{(-)}(z)\right) &= 2\sum_{l=0}^{\infty}\left(a_l^{(+)}(z) - a_l^{(-)}(z)\right)C_{m,l}(z) \end{aligned} \tag{4.21}$$

By taking the sum or the difference in Eq. (4.21), we obtain

$$\frac{\partial a_m^{(+)}(z)}{\partial z} - i\beta_m a_m^{(+)}(z) = \sum_{l=0}^{\infty} a_l^{(+)}(z)\big(K_{m,l}(z) + C_{m,l}(z)\big) + \sum_{l=0}^{\infty} a_l^{(-)}(z)\big(K_{m,l}(z) - C_{m,l}(z)\big)$$
$$\frac{\partial a_m^{(-)}(z)}{\partial z} + i\beta_m a_m^{(-)}(z) = \sum_{l=0}^{\infty} a_l^{(+)}(z)\big(-K_{m,l}(z) + C_{m,l}(z)\big) + \sum_{l=0}^{\infty} a_l^{(-)}(z)\big(-K_{m,l}(z) - C_{m,l}(z)\big) \tag{4.22}$$

By using Eq. (4.20), we can get the mode equations for the slowly varying factors $c_m^{(\pm)}$ as

$$\frac{\partial c_m^{(+)}(z)}{\partial z} = \sum_{l=0}^{\infty}\big(K_{m,l}(z) + C_{m,l}(z)\big)c_l^{(+)}(z)e^{i(\beta_l-\beta_m)z} + \sum_{l=0}^{\infty}\big(K_{m,l}(z) - C_{m,l}(z)\big)c_l^{(-)}(z)e^{(-i\beta_l-\beta_m)z}$$
$$\frac{\partial c_m^{(-)}(z)}{\partial z}e^{-i\beta_m z} = \sum_{l=0}^{\infty}\big(-K_{m,l}(z) + C_{m,l}(z)\big)c_l^{(+)}(z)e^{i(\beta_l+\beta_m)z} + \sum_{l=0}^{\infty}\big(-K_{m,l}(z) - C_{m,l}(z)\big)c_l^{(-)}(z)e^{(-i\beta_l+i\beta_m)z} \tag{4.23}$$

To simplify the expression, we define the coupling coefficient as:

$$\chi_{m,l}^{(p,q)}(z) = pK_{m,l}(z) + qC_{m,l}(z)$$
$$= \frac{i\omega\varepsilon_0}{4P}\int\left(\left(n^2(\vec{r}) - n_0^2(x,y)\right)\times\left(p\frac{|\beta_m|}{\beta_m}\vec{E}_{m,t}^*(x,y)\cdot\vec{E}_{l,t}(x,y) + q\frac{|\beta_m|}{\beta_m^*}\frac{n_0^2(x,y)}{n^2(\vec{r})}\vec{E}_{m,z}^*(x,y)\cdot\vec{E}_{l,z}(x,y)\right)\right)da \tag{4.24}$$

where $p, q = \pm$. Then we will finally obtain the coupled mode equation for $c_m^{(\pm)}$ as

$$\frac{\partial c_m^{(+)}(z)}{\partial z} = \sum_{l=0}^{\infty}\chi_{m,l}^{(+,+)}c_l^{(+)}(z)e^{i(\beta_l-\beta_m)z} + \sum_{l=0}^{\infty}\chi_{m,l}^{(+,-)}c_l^{(-)}(z)e^{(-i\beta_l-\beta_m)z}$$
$$\frac{\partial c_m^{(-)}(z)}{\partial z} = \sum_{l=0}^{\infty}\chi_{m,l}^{(-,+)}c_l^{(+)}(z)e^{i(\beta_l+\beta_m)z} + \sum_{l=0}^{\infty}\chi_{m,l}^{(-,-)}c_l^{(-)}(z)e^{(-i\beta_l+i\beta_m)z} \tag{4.25}$$

From Eq. (4.25), we can obtain the coupling mode equation for FBGs and LPGs by considering the refractive index profile of the perturbed waveguide $n(\vec{r})$as:

$$n(\vec{r}) = n_0(x,y) + \Delta n(\vec{r}) \tag{4.26}$$

If the perturbation is small such that $\Delta n \ll n_0$, we can approximate Eq. (4.26) as since $\Delta n^2 \to 0$:

$$n^2(\vec{r}) \approx n_0^2(x,y) + 2n_0(x,y)\Delta n(\vec{r}). \tag{4.27}$$

In conventional waveguides, most of lower guided modes have small propagating angles. Therefore the amplitude of the longitudinal field in the z-direction is much smaller than that of the transverse field in the x- and y-direction. Therefore, we can conclude:

$$\begin{aligned} \left|\vec{E}_t\right| &\gg \left|\vec{E}_z\right| \\ \left|\vec{H}_t\right| &\gg \left|\vec{H}_z\right| \\ \left|K_{m,l}(z)\right| &\gg \left|C_{m,l}(z)\right| \end{aligned} \tag{4.28}$$

Then, the coupling constant can be modified as

$$\begin{aligned} \chi_{m,l}^{(p,q)}(z) &= pK_{m,l}(z) + qC_{m,l}(z) \approx pK_{m,l}(z) \\ &= p\frac{i\omega\varepsilon_0}{4P}\iint 2n_0(x,y)\Delta n(\vec{r})\vec{E}_{m,t}^{*}(x,y)\cdot\vec{E}_{l,t}(x,y)da \end{aligned} \tag{4.29}$$

By considering that the index perturbation is uniformly induced across the cross sectional area of the waveguide in the z-direction but restricted in a localized area, Eq. (4.29) can be written as:

$$\begin{aligned} K_{m,l}(z) &= i2\Delta n(z)\Omega_{m,l} \\ \Omega_{m,l} &= \frac{i\omega\varepsilon_0}{4P}\iint 2n_0(x,\,y)\Delta n(\overrightarrow{r})\,E_{m,t}^{*}(x,\,y)\cdot\ \overrightarrow{E}_{l,t}(x,\,y)da \end{aligned} \tag{4.30}$$

where $\Omega_{m,l} = \Omega_{m,l}^{*}$. Therefore, $\Omega_{m,l}$ is real in general.

For the case of fiber gratings, the index perturbation can be written as

$$\Delta n(z) = \Delta n_{dc}(z) + \Delta n_{dc}(z)Cos(Kz + \Phi(z)) \tag{4.31}$$

where $\Delta n_{dc}(z)$ is a slowly varying DC part ($\sim$ average index variation) and $\Delta n_{ac}(z)$ is the rapidly varying AC part with a small phase variation, $\Phi(z)$.

4.1.1 LPG: Co-Directional Coupling with Sinusoidal Perturbation

From Eqs. (4.25) and (4.30), the coupled equations for the co-directional case can be written as:

$$\frac{\partial c_m^{(+)}(z)}{\partial z} = \sum_{l=0}^{\infty}\chi_{ml}^{(+,+)}(z)e^{i(\beta_l-\beta_m)z} \approx 2i\Delta n(z)\sum_{l=0}^{\infty}\Omega_{ml}^{(+)}c_l^{(+)}(z)e^{i(\beta_l-\beta_m)z} \tag{4.32}$$

By inserting the periodic variation of Eq. (4.31) and decomposing it with self coupling terms and cross coupling terms, we obtain:

$$\begin{aligned} \frac{\partial c_m^{(+)}(z)}{\partial z} =& 2i[\Delta n_{dc}(z) + \Delta n_{ac}(z)\cos(Kz + \Phi(z))]\Omega_{m,m}^{(+)}c_m^{(+)}(z) \\ &+2i[\Delta n_{dc}(z) + \Delta n_{ac}(z)\cos(Kz + \Phi(z))]\sum_{l\neq m}\Omega_{ml}^{(+)}c_l^{(+)}(z)e^{i(\beta_l-\beta_m)z} \end{aligned}, \tag{4.33}$$

The cosine function can expressed in terms of exponential functions:

$$\cos(Kz + \Phi(z)) = \frac{1}{2}\left(e^{i\phi(z)}e^{iKz} + e^{-i\phi(z)}e^{-iKz}\right) \tag{4.34}$$

Substituting Eq. (4.34) into Eq. (4.35) gives

$$\begin{aligned}\frac{\partial c_m^{(+)}(z)}{\partial z} &= 2i\Delta n_{dc}(z)\Omega_{m,m}^{(+)}c_m^{(+)}(z) \\ &+ i\Delta n_{ac}(z)e^{i\phi(z)}\Omega_{m,m}^{(+)}c_m^{(+)}(z)e^{iKz} \\ &+ i\Delta n_{ac}(z)e^{-i\phi(z)}\Omega_{m,m}^{(+)}c_m^{(+)}(z)e^{-iKz} \\ &+ 2i\Delta n_{dc}(z)\sum_{l\neq m}\Omega_{m,l}^{(+)}c_l^{(+)}(z)e^{i(\beta_l-\beta_m)z} \\ &+ i\Delta n_{ac}(z)e^{i\phi(z)}\sum_{l\neq m}\Omega_{m,l}^{(+)}c_l^{(+)}(z)e^{i(\beta_l-\beta_m+K)z} \\ &+ i\Delta n_{ac}(z)e^{-i\phi(z)}\sum_{l\neq m}\Omega_{m,l}^{(+)}c_l^{(+)}(z)e^{i(\beta_l-\beta_m-K)z}\end{aligned} \tag{4.35}$$

Since each c_m is the slowly varying modal amplitude, the effect made by the rapidly varying (or oscillating) terms in the above equation can be neglected in most cases. Also for simplicity let's only consider the mode coupling between the core and the co-propagating cladding modes in a single-mode fiber, therefore:

$$c_m^{(+)} = c_{core}, c_{cadd}^{v}(for\ v = 1, 2, 3, 4, \ldots) \tag{4.36}$$

The effective index of the core mode is greater than that of the cladding modes ($\beta_{core} > \beta_{clad}^{v}$ for any cladding of mode order, v). The grating contains many periods within the length of the grating, d. Then, we can get $Kd \gg 1$, with $K = 2\pi/\Lambda$, Λ is the grating period. The mode spacing of the cladding modes is wide enough or/and the length of the grating is long enough to satisfy:

$$\left(\beta_{clad}^{v} - \beta_{clad}^{v+1}\right)d \gg 1 \tag{4.37}$$

The coupling coefficient between cladding modes is extremely small. The terms with the following phase factors in Eq. (4.35) can be sufficiently small to be neglected;

$$e^{iKz},\ e^{-iKz},\ e^{i\left(\beta_{core}-\beta_{clad}^{v}\right)z} \tag{4.38}$$

Therefore, only three terms (one self term and two sets of cross terms) are remained;

$$\begin{aligned}\frac{\partial c_m^{(+)}(z)}{\partial z} &\approx 2i\Delta n_{dc}(z)\Omega_{mm}^{(+)}c_m^{(+)}(z) \\ &+ i\Delta n_{ac}(z)se^{i\Phi(z)}\sum_{l\neq m}\Omega_{ml}^{(+)}c_l^{(+)}(z)e^{i(\beta_l-\beta_m+K)z} \\ &+ i\Delta n_{ac}(z)e^{-i\Phi(z)}\sum_{l\neq m}\Omega_{ml}^{(+)}c_l^{(+)}(z)e^{i(\beta_l-\beta_m-K)z},\end{aligned} \tag{4.39}$$

Decomposing Eq. (4.39) (when the left side is the core mode), we can obtain the coupled core mode with a certain mode order (v) as:

$$\begin{aligned}\frac{\partial c_{core}(z)}{\partial z} &\approx 2i\Delta n_{dc}(z)\Omega_{core,core}^{(+)}c_{core}(z) \\ &+ i\Delta n_{ac}(z)e^{i\Phi(z)}\sum_{v}\Omega_{core,v}^{(+)}c_{clad}^{v}(z)e^{i\left(\beta_{clad}^{v}-\beta_{core}+K\right)z} \\ &+ i\Delta n_{ac}(z)e^{-i\Phi(z)}\sum_{v}\Omega_{core,v}^{(+)}c_{clad}^{v}(z)e^{i\left(\beta_{clad}^{v}-\beta_{core}-K\right)z}\end{aligned} \tag{4.40}$$

In the 2-nd term, the phase factor can be vanished only for one cladding mode that satisfies the phase matching condition defined as

$$\Delta\beta \equiv \beta_{core} - \beta_{clad}^{v} - K \rightarrow 0 \tag{4.41}$$

Then we can obtain the expression for the phase matching condition for the LPG as

$$\lambda_p = \Lambda(n_{core} - n_{clad}^{v}) \tag{4.42}$$

Note that for a given waveguide, the order of cladding mode (v) for the mode coupling is determined (or selected) by the amount of K. The phase of the last term of Eq. (4.40) is typically sufficiently small enough to be neglected, therefore Eq. (4.40) can be written as:

$$\frac{\partial c_{core}(z)}{\partial z} \approx 2i\Delta n_{dc}(z)\Omega_{core,core}^{(+)}c_{core}(z) + i\Delta n_{ac}(z)e^{i\Phi(z)}\Omega_{core,v}^{(+)}c_{clad}^{v}(z)e^{-i\Delta\beta z} \tag{4.43}$$

By using the same procedure, the coupling mode equation can be obtained as

$$\frac{\partial c_{clad}^{v}(z)}{\partial z} \approx 2i\Delta n_{dc}(z)\Omega_{v,v}^{(+)}c_{clad}^{v}(z) + i\Delta n_{ac}(z)e^{-i\Phi(z)}\Omega_{v,core}^{(+)}c_{core}(z)e^{i\Delta\beta z}, \tag{4.44}$$

By defining the coupling constant κ as

$$\kappa_{dc}^{co} \equiv 2\Delta n_{dc}\Omega_{core,core}^{(+)} \quad \text{and} \quad \kappa_{dc}^{cl} \equiv 2\Delta n_{dc}\Omega_{v,v}^{(+)}$$

$$\kappa = \kappa_{ac} \equiv \Delta n_{ac}\Omega_{core,v}^{(+)}, \quad \text{Then,} \quad \Delta n_{ac}\Omega_{v,core}^{(+)} = \kappa_{ac}^{*} \equiv \kappa^{*}$$

And re-defining the mode indexing as

$$A = A(z) \equiv c_{core}(z) \quad \text{Core mode amplitude (slowly varying)}$$

$$B = B(z) \equiv c^{v}_{clad}(z) \quad \text{Cladding mode amplitude (slowly varying)}$$

Then, the coupled mode equation becomes

$$A' = i\kappa^{co}_{dc}A + i\kappa_{ac}Be^{-i\Delta\beta z} \tag{4.45}$$

$$B' = i\kappa^{*}_{ac}Ae^{+i\Delta\beta z} + i\kappa^{cl}_{dc}B \tag{4.46}$$

In a matrix form, it can be written as:

$$\begin{bmatrix} A(z)' \\ B(z)' \end{bmatrix} = i\begin{bmatrix} \kappa^{co}_{dc} & \kappa_{ac}e^{-i\Delta\beta z} \\ \kappa^{*}_{ac}e^{+i\Delta\beta z} & \kappa^{cl}_{dc} \end{bmatrix}\begin{bmatrix} A(z) \\ B(z) \end{bmatrix} \tag{4.47}$$

The solution of the coupled-mode equation of two co-propagating modes is then given by

$$\begin{bmatrix} A(z) \\ B(z) \end{bmatrix} = e^{i\frac{\beta_{co}+\beta^{v}_{cl}}{2}z}\begin{bmatrix} \left(\cos sz + i\frac{\Delta\beta}{2s}\sin sz\right)e^{i\frac{K}{2}z} & i\frac{\kappa}{s}e^{i\frac{K}{2}z}\sin sz \\ i\frac{\kappa*}{s}e^{-i\frac{K}{2}z}\sin sz & \left(\cos sz - i\frac{\Delta\beta}{2s}\sin sz\right)e^{-i\frac{K}{2}z} \end{bmatrix}\begin{bmatrix} A(0) \\ B(0) \end{bmatrix} \tag{4.48}$$

where s is $\sqrt{\left(\frac{\Delta\beta}{2}\right)^2 + \kappa\kappa*}$.

4.1.2 FPG: Co-Directional Coupling with Sinusoidal Perturbation

A core mode can be coupled to a counter propagating mode by a periodic index perturbation that exists in FBGs. Since single- mode fibers have only one core mode with a mode order l, only $c_1^{(\pm)}$ modes are possibly confined. Thus, from Eq. (4.25) we can obtain:

$$\frac{\partial c_1^{(+)}(z)}{\partial z} = \chi_{11}^{(+,+)}(z)c_1^{(+)}(z)e^{i(\beta_1-\beta_1)z} + \chi_{11}^{(+,-)}(z)c_1^{(-)}(z)e^{i(-\beta_1-\beta_1)z} \tag{4.49}$$

$$\frac{\partial c_m^{(-)}(z)}{\partial z} = \chi_{m1}^{(-,+)}(z)c_1^{(+)}(z)e^{i(\beta_1+\beta_1)z} + \chi_{m1}^{(-,-)}(z)c_1^{(-)}(z)e^{i(-\beta_1+\beta_m)z} \tag{4.50}$$

Since the mode order m becomes 1 in the FBG, Eqs. 4.48 and 4.49 become

$$\frac{\partial c_1^{(+)}(z)}{\partial z} = \chi_{11}^{(+,+)}(z)c_1^{(+)}(z) + \chi_{11}^{(+,-)}(z)c_1^{(-)}(z)e^{-2i\beta_1 z} \tag{4.51}$$

$$\frac{\partial c_1^{(-)}(z)}{\partial z} = \chi_{11}^{(-,+)}(z)c_1^{(+)}(z)e^{+2i\beta_1 z} + \chi_{11}^{(-,-)}(z)c_1^{(-)}(z) \tag{4.52}$$

Using the new coupling coefficient defined in Eq. (4.30) yields

$$\chi_{11}^{(p,q)}(z) \approx i2\Delta n(z)\Omega_{11}^{p} = pi2\Delta n(z)\Omega_{11} \tag{4.53}$$

$$\Omega_{11}^{p} \equiv p\frac{\omega\varepsilon_0}{4P}\frac{|\beta_1|}{\beta_1}\iint_{pert} n_0(x,y)\mathrm{E}_{1t}^{*}(x,y)\cdot\mathrm{E}_{1t}(x,y)dxdy \tag{4.54}$$

$$\equiv p\frac{\omega\varepsilon_0}{4P}\frac{|\beta_1|}{\beta_1}\iint_{pert} n_0(x,y)|\mathrm{E}_{1t}(x,y)|^2 dxdy, \tag{4.55}$$

with $\Omega_{11}^{(-)} = -\Omega_{11}^{(+)}$. The coupling intensity is proportional to the intensity of E field of the core mode. With the sinusoidal index variation of Eq. (4.31), we have:

$$\begin{aligned}\frac{\partial c_1^{(+)}(z)}{\partial z} &= 2i\Delta n_{dc}(z)\Omega_{11}^{(+)}c_1^{(+)}(z) \\ &\quad + i\Delta n_{ac}(z)\Omega_{11}^{(+)}c_1^{(-)}(z)\left[e^{-i\Phi(z)}e^{i(-2\beta_1-\mathrm{K})z} + e^{i\Phi(z)}e^{i(-2\beta_1+\mathrm{K})z}\right]\end{aligned} \tag{4.56}$$

$$\begin{aligned}\frac{\partial c_1^{(-)}(z)}{\partial z} &= i\Delta n_{ac}(z)\Omega_{11}^{(-)}c_1^{(+)}(z)\left[e^{-i\Phi(z)}e^{i(2\beta_1-\mathrm{K})z} + e^{i\Phi(z)}e^{i(2\beta_1+\mathrm{K})z}\right] \\ &\quad + 2i\Delta n_{dc}(z)\Omega_{11}^{(-)}c_1^{(-)}(z)\end{aligned} \tag{4.57}$$

The terms having phases of $e^{\pm i\mathrm{K}z}$ and $e^{\pm i2\beta_1}$ can be sufficiently small to be neglected. The coupling factors of the core mode to other co-directional modes were also removed for a single core fiber. Only the terms having small phase factors dominates the coupling that is $\Delta\boldsymbol{\beta} \equiv 2\boldsymbol{\beta}_{core} - \mathbf{K} \rightarrow \boldsymbol{0}$.

Then we obtain the expression for the phase matching condition for the FBG as

$$\lambda_p = 2n_{core}\Lambda \tag{4.58}$$

For the case of a uniform grating ($\Phi(z) = 0$), we can write the coupled mode equation for the FBG as:

$$\frac{\partial c_1^{(+)}(z)}{\partial z} = 2i\Delta n_{dc}(z)\Omega_{11}^{(+)}c_1^{(+)}(z) + i\Delta n_{ac}(z)\Omega_{11}^{(+)}c_1^{(-)}(z)e^{-i\Delta\beta z} \tag{4.59}$$

$$\frac{\partial c_1^{(-)}(z)}{\partial z} = i\Delta n_{ac}(z)\Omega_{11}^{(-)}c_1^{(+)}(z)e^{+i\Delta\beta z} + 2i\Delta n_{dc}(z)\Omega_{11}^{(-)}c_1^{(-)}(z) \tag{4.60}$$

Here the coupling constant$\kappa$and the mode indexing can be defined as

$$\kappa_{dc}(z) \equiv 2\Delta n_{dc}(z)\Omega_{11}^{(+)}$$

$$\kappa_{ac}(z) \equiv \Delta n_{ac}(z)\Omega_{11}^{(+)}$$

$$A = A(z) \equiv c_1^{(+)}(z)$$

$$B = B(z) \equiv c_1^{(-)}(z)$$

by using the relationship of $\Omega_{11}^{(-)} = -\Omega_{11}^{(+)}$, we have the coupled mode equations for two counter-propagating modes as

$$\frac{\partial A(z)}{\partial z} = i\kappa_{dc}(z)A(z) + i\kappa_{ac}(z)B(z)e^{i\Delta\beta z} \tag{4.61}$$

$$\frac{\partial B(z)}{\partial z} = -i\kappa_{ac}^{*}(z)A(z)e^{-i\Delta\beta z} - i\kappa_{dc}(z)B(z) \tag{4.62}$$

with $\Delta\beta \equiv 2\beta_{core} - \mathrm{K}$

This can be written in a matrix form as:

$$\begin{bmatrix} A(z)' \\ B(z)' \end{bmatrix} = i\begin{bmatrix} \kappa_{dc} & \kappa_{ac}e^{-i\Delta\beta z} \\ -\kappa_{ac}^{*}e^{+i\Delta\beta z} & -\kappa_{dc} \end{bmatrix}\begin{bmatrix} A(z) \\ B(z) \end{bmatrix} \tag{4.63}$$

The solution of the coupled-mode equation of two counter propagating modes is given by

$$\begin{bmatrix} A(z) \\ B(z) \end{bmatrix} = \begin{bmatrix} \left(\cosh sz + i\frac{\Delta\beta}{2s}\sinh sz\right)e^{i\frac{K}{2}z} & i\frac{\kappa}{s}e^{i\frac{K}{2}z}\sinh sz \\ -i\frac{\kappa*}{s}e^{-i\frac{K}{2}z}\sinh sz & \left(\cosh sz - i\frac{\Delta\beta}{2s}\sinh sz\right)e^{-i\frac{K}{2}z} \end{bmatrix}\begin{bmatrix} A(0) \\ B(0) \end{bmatrix} \tag{4.64}$$

where s is $\sqrt{\kappa\kappa* - \left(\frac{\Delta\beta}{2}\right)^2}$.

4.2 Application I: Optical Delay Control

Chirped FBGs can be used to precisely control the optical delay and this can be used for applications in telecommunication, fiber-optic sensors, microwave photonics, and bio-imaging. Chirped fiber Bragg gratings (CFBGs) have been used for dispersion compensating devices due to their fiber compatibility, polarization insensitivity, low nonlinearity, low loss and so on [6]. By compensating dispersion in optical systems, high quality optical signal transmission was realized [7, 8]. Multiple elements photonic microwave true-time delay beam-forming based on the chirped FBGs was achieved [9]. High speed and real time optical imaging technique was also obtained by using chirped FBGs [10]. The most important property of the chirped FBGs is that it can control the optical delay time without center wavelength shift. A simple and convenient method to control the optical delay time is to exploit a symmetrical bending apparatus [11]. When the linear strain like the tension or compression strain is induced along the length of a fiber grating, the resonant wavelength is shifted into the longer and shorter wavelength,

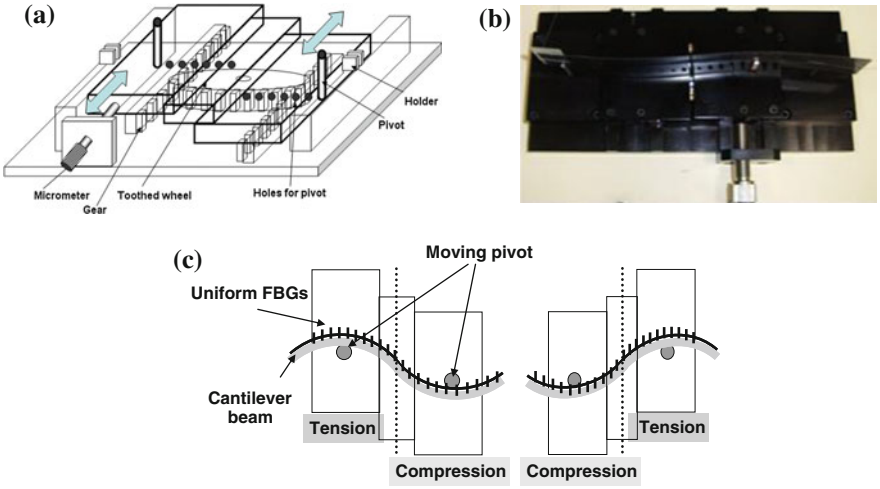

Fig. 4.3 **a** Schematic of a chromatic dispersion controller with a uniform FBG. **b** Photograph of the fabricated bending apparatus. **c** Symmetrical bending scheme based on two moving stage. Tension and compression strain depending on the bending direction can be induced [11]

respectively, Consequently, the chirp ratio of uniform FBG is changed by the tension and compression strain induced by the symmetrical bending, but the center wavelength is not changed because the effect of tension and compression strain on the center wavelength shift should be compensated mutually. Therefore, the group delay and dispersion can be controlled without the center wavelength shift.

Figures 4.3a and b show the experimental scheme and the photograph for the symmetrical bending apparatus, respectively, to control the optical delay time with a uniform FBG [11]. The sophisticated fiber bending can induce symmetrically linear strains gradient in the center of the uniform FBG. It consists of two translation stages with gears, a sawtooth wheel, two pivots, a micrometer, and two cantilever beam holder. Opposite movement of two translation stages with gears converts the linear motion of translation stage into the rotary motion of sawtooth wheel. Figure 4.3c shows the induction principle of tension and compression strain along the uniform FBG depending on the bending direction. When the left translation stage is moved forward by the micrometer, its gear rotates the sawtooth wheel and the right translation stage is moved backward by the rotary motion of the sawtooth wheel. As two translation stages are moved oppositely by the interaction between two gears and a sawtooth wheel, the position of two pivots on two translation stages is changed oppositely, which induces the symmetrical bending along the flexible cantilever beam. Consequently the tension and compression strain along the uniform FBG through the symmetrically curved cantilever beam corresponding to the bending direction can be induced. Therefore, the optical time delay of the uniform FBG can be effectively controlled by inducing the tension and compression strain at each side of the FBG without the center wavelength shift.

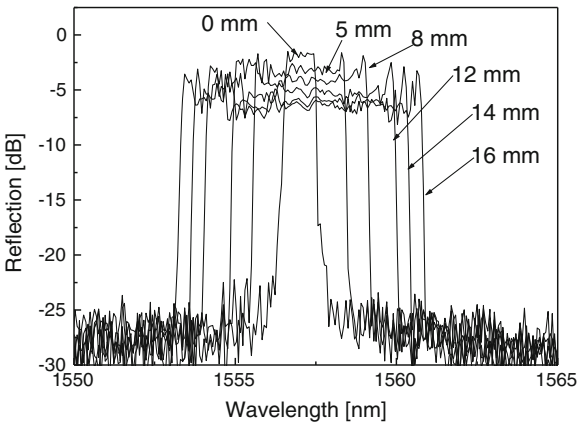

Fig. 4.4 Measured reflection spectra as a function of the variations in the translation stage moving distance [11]

The flexible cantilever beam is made of a spring steel with the high resistance against fatigue and corrosion. The uniform FBG was carefully attached to the cantilever beam using the UV curable epoxy to reduce the phase error along the fiber grating due to the microbending, which can induce additional phase error. The uniform FBG was apodized by using the Blackman profile to reduce the sidelobes and the group delay ripple [7].

Figure 4.4 shows the experimentally obtained reflection spectra of the uniform FBG as a function of the variations in the moving distance of the translation stage. As the micrometer moves, the bending curve along the cantilever beam becomes larger and this increases the amount of tension and compression strain corresponding to the bending direction. A large amount of strain gradient changes the chirp ratio along the uniform FBG and consequently makes its bandwidth be broad without the center wavelength shift.

Figures 4.5a and b show the measured group delay and the measured group velocity dispersion of the uniform FBG with the variation of the translation stage. When the left translation stage was changed, the dispersion of CFBG was controlled in the range from 312.6 ps/nm to 35.9 ps/nm. The small difference between two results may be caused by the imperfection in the fabrication of the grating or in curing process and coating material. The group delay ripple and the amplitude of group delay ripple were successfully reduced, which was measured to be less than $\sim \pm 5$ ps over the whole dispersion tuning range. Since the uniform FBG apodized by the Blackman profile was utilized, the stitching error induced by the imperfection of the phase mask could be removed and the group delay ripple could be suppressed. It is obvious that the uniform FBG is more effective for achieving tunable chromatic dispersion control compared to using the chirped FBG.

Compared to FBGs, LPGs have an advantage of being able to be mass produced due to their large periodicity and the nature of amplitude masks [1]. Therefore, LPGs have potential for various applications, for example, gain flattening of erbium doped fiber amplifier (EDFA), band-rejection filters [1]. Additionally, LPGs is attracting interest for applications in sensing strain and temperature due to

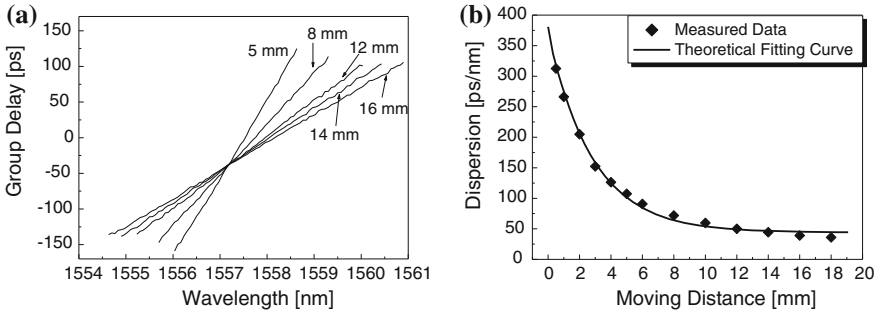

Fig. 4.5 (**a**) Measured group delay and (**b**) group velocity dispersion with variations in the moving distance of the translation stage [11]

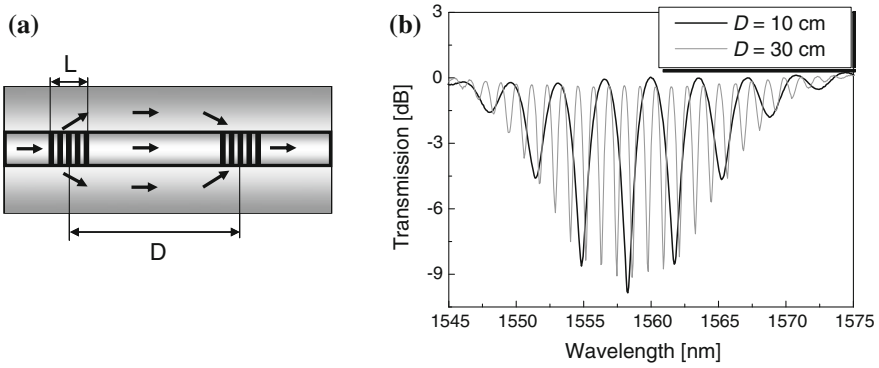

Fig. 4.6 **a** Operating principle of the cascaded LPFG resulting in the interference between the core and cladding modes. (**b**) transmission spectra of the cascaded LPGs with different separation distances [22]

its high sensitivity to these parameters [2]. LPGs are usually fabricated with the amplitude mask method or the point-by-point method. Based on these methods, several techniques have been developed for fabrication of the LPGs: (1) irradiation of UV laser beam on hydrogen-loaded GeO_2-doped fibers with the photosensitivity effect [1]; (2) periodic relaxation of residual stress with CO_2 laser [12, 13]; (3) periodic physical deformation of the core with electric arc, CO_2 laser, and flame [14–16]; (4) microbending with electric arc [17]; and (5) thermal diffusion in nitrogen-doped silica-core fiber with electric arc or CO_2 laser [18]. Several mechanisms, e.g., color center model [19] and residual stress relief model [20], have been proposed for explanation of the refractive index change.

It is possible to realize the true time delay based on the cascaded LPGs [21]. As seen in Fig. 4.6, the interference pattern resulting from the interaction between the core and the cladding modes in two identical LPGs must be generated [22]. Optical properties of the cascaded LPGs, such as peak spacing, bandwidth, and the number of peaks, are controlled by changing physical parameter, such as the length of a

LPG, the separation distance between two LPGs, the number of LPGs [22]. The differential group delay ($\Delta\tau$) in the cascaded LPGs can be derived by [21]

$$\Delta\tau = \frac{1}{c}(n_{Co} - n_{Cl}^{m} - \lambda\frac{d}{d\lambda}(n_{Co} - n_{Cl}^{m})), \tag{4.65}$$

where c is the light velocity and n_{Co} and n_{Cl}^{m} are effective indices of the core and the cladding modes, respectively. m is the cladding mode order. If a single pulse in time domain propagates along the cascaded LPGs, the first LPG divides a single pulse into several pulses, which have different delays. Since the effective index of the cladding is lower than that of the core, the optical pulse in the cladding mode propagates faster than that in the core mode. As seen in Eq. (4.65), it is clearly obvious that the amount of $\Delta\tau$ is dominantly determined by the differential effective group index between the core and the cladding modes in a single-mode fiber. However, the optical time delay induced by the cascaded LPGs is very short ($\sim$11.8 ps/m [21]) because of the small difference of the effective refractive indices.

4.3 Application II: Mechanical Sensors

Fiber gratings, in general, have high sensitivity to external perturbation such as temperature, strain and bending, which have also led to much interest for sensing applications [2]. The liquid level sensor based on phase shifting of LPGs induced by the ambient refractive index was reported [23, 24] and the application of the peak splitting of LPGs to bend sensors was reported [25, 26]. These sensors, however, have limitations, such as concurrent sensitivities to multiple perturbations; e.g., strain and temperature or bending and temperature. Versatile methods of discriminating two coexisting sensitivities have been proposed, including combination of two fiber Bragg gratings (FBGs) with different cladding diameter [27] FBG-based practical sensors including a supplementary bending cantilever beam were proposed as a promising solution for another simultaneous measurement of pressure and temperature [28] and for measuring displacement and temperature [29]. A single sampled chirped FBG (CFBG) embedded on a flexible cantilever beam is capable of discriminating bending and temperature sensitivities [30]. The sampled CFBG has multiple resonant peaks corresponding to the chirp ratio and the number of grating samples. Figure 4.7(a) and 4.7(b) show the scheme for the sensing probe and the transmission spectrum of a sampled CFBG embedded on a cantilever beam for simultaneous measurement of bending and temperature. The sampled CFBG was fabricated after exposing a photosensitive fiber to a 244 nm Ar+ laser beam through a chirped phase mask. The UV laser was periodically opened and closed by using a shutter to modulate the amplitude of the UV-induced refractive index resulting in the formation of the sampled CFBG. Then the sampled CFBG was carefully attached to the cantilever beam by using the UV curable epoxy [30].

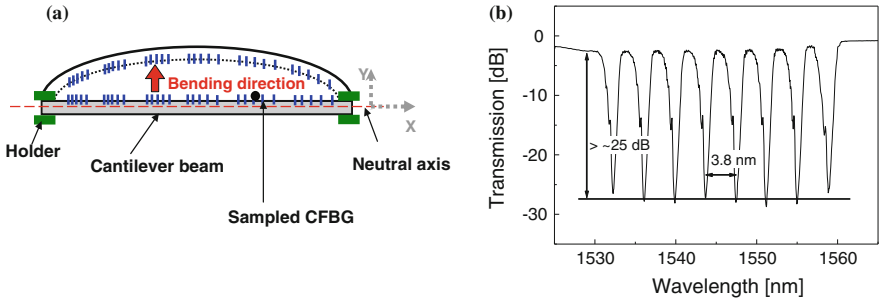

Fig. 4.7 **a** Scheme for the sensing probe based on a sampled CFBG embedded on a cantilever beam for simultaneous measurement of bending and temperature. **b** Transmission spectrum of the sampled CFBG [30]

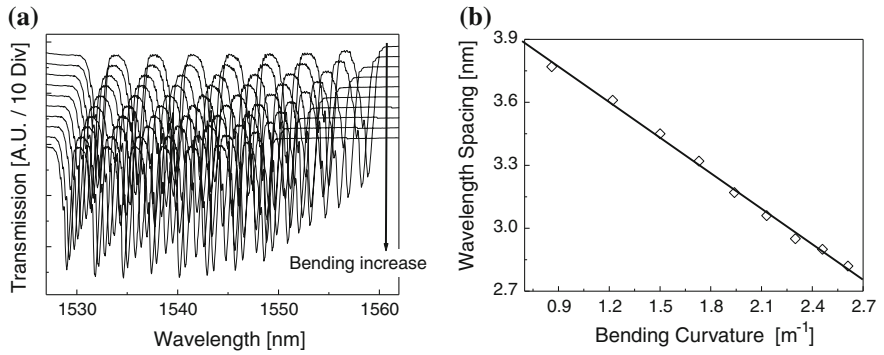

Fig. 4.8 **a** Transmission spectra of the sampled CFBG. **b** Wavelength spacing change as a function of the bending curvature change [30]

When the external bending is applied to the sampled CFBG, the wavelength spacing of the sampled CFBG is changed because the compressive strain gradient induced by the bending of the cantilever beam modifies the chirp ratio of the chirped FBG. However, the wavelength spacing of the fiber grating is not changed by the applied temperature because the chirp ratio of the sampled CFBG is not changed by variation in temperature. The multiple resonant wavelengths, however, are only shifted into the longer wavelength due to the positive thermal expansion and optic coefficients of the fiber grating [30].

Figure 4.8a shows the transmission spectra of the sampled CFBG with variations in the bending curvature. Since the compression strain gradient induced by the bending reduces the chirp ratio of the sampled CFBG, the wavelength spacing diminishes as the bending curvature increases. It should be manifest that the multiple resonant peaks also shift into the shorter wavelength due to the compression strain along the sampled CFBG [30].

Figure 4.9(a) shows the transmission spectra of the sampled CFBG as the applied temperature changes. Figuress 4.9(b) and 4.9(c) show the multiple

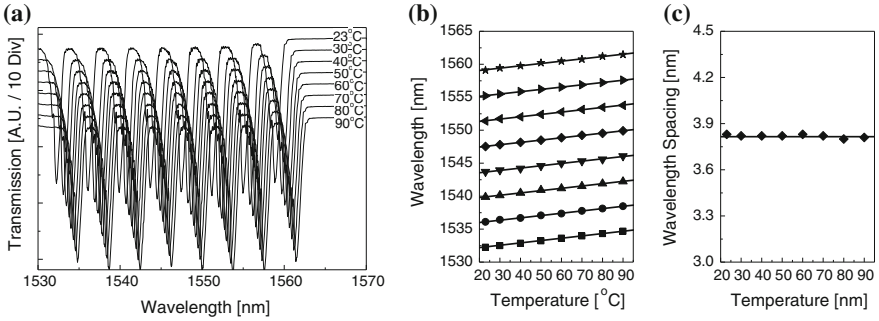

Fig. 4.9 **a** Transmission spectra of the sampled CFBG, **b** multiple resonant wavelength shifts, and (c) wavelength spacing change as a function of temperature, respectively [30]

resonant wavelength shifts and the wavelength spacing change as a function of temperature, respectively. All of multiple resonant wavelengths were shifted into the longer wavelength due to the positive thermal expansion and optic coefficient of the photosensitive fiber with high concentration of germanium. The wavelength spacing, however, was not changed by the applied temperature because of the independence of the chirp ratio on the ambient temperature variation [30].

In general, the cladding modes coupled from the core mode in the LPGs is directly interfaced with external environment. It means that the LPGs have higher sensitivity to the external perturbation than FBGs in terms of temperature sensitivity. The temperature sensitivity of LPGs is changed by controlling the doping concentrations of GeO_2 and B_2O_3 in the core region. The deviation of the waveguide property due to temperature variation ($d\Lambda/dT$) is negligible compared to that of the material property (dn/dT), and the temperature dependence of the resonance peak wavelength can be written as [31]

$$\frac{d\lambda}{dT} \approx \Lambda\left(\frac{dn_{Co}}{dT} - \frac{dn_{Cl}^{m}}{dT}\right) \tag{4.66}$$

It is obvious that the temperature sensitivity of the LPG can be controlled by adjusting dopants, such as B_2O_3 with negative thermal property. For example, the temperature sensitivity can be decreased by increasing the doping concentration of B_2O_3 in the core. On the other hand, the temperature sensitivity can be positively enhanced by doping B_2O_3 in the inner cladding [31].

Two kinds of single-mode fibers with similar properties except the doping concentrations of GeO_2 and B_2O_3 were exploited to fabricate LPGs with UV excimer laser. The physical parameters of the two fibers are: core diameter = 3.6 μm and 3.8 μm, relative index difference = 1.0 % and 0.8 %, cut off wavelength = 960 nm and 910 nm. The cladding diameter is 125 μm for both. The length and the period of the LPG were 1.17 mJ/mm^2, 2 cm, and 400 μm, respectively. The temperature and strain sensitivities of two LPGs for several cladding mode orders (m) were then measured, and the measurement results are shown in Table 4.1. LPG1 and LPG2 have positive and negative temperature sensitivities,

Table 4.1 Temperature and strain sensitivities of LPG1 and LPG2 with the cladding mode order (m) [31]

	LPG1			LPG2		
	$HE_{1,3}$	$HE_{1,4}$	$HE_{1,5}$	$HE_{1,3}$	$HE_{1,4}$	$HE_{1,5}$
Wavelength [nm]	1217.27	1303.13	1488.86	1393.52	1488.86	1681.35
$d\lambda/dT$ [nm/ °C]	0.06	0.07	0.10	−0.57	−0.59	−0.65
$d\lambda/d\varepsilon$ nm/μstrain]	0.41	0.42	0.46	0.43	0.46	0.51

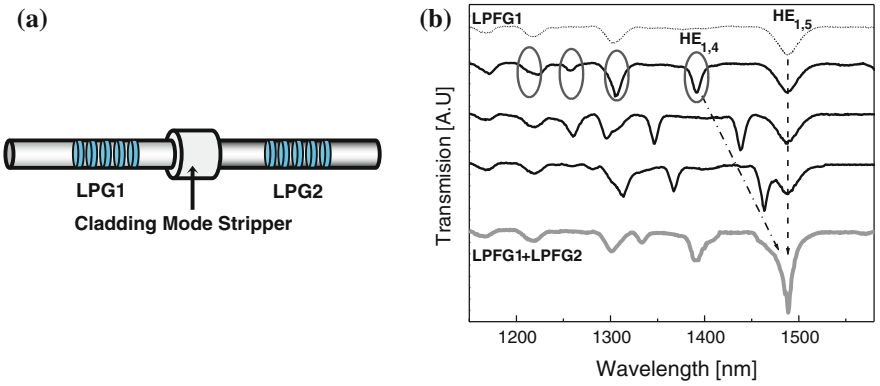

Fig. 4.10 **a** Scheme for the sensing probe based on two LPGs with similar strain sensitivities for the simultaneous measurement of strain and temperature. **b** Evolution of the transmission characteristics of two LPGs during the grating formation. [31]

respectively. The data also indicates that the temperature and strain sensitivities of LPG1 and LPG2 vary with the cladding mode order. The strain sensitivity of LPGs depends on the strain-optic coefficient, grating period Λ, and the cladding mode order [2]. In previous reports, it was shown that the strain sensitivity of LPG increases with the cladding mode order [2]. The strain sensitivity of the $HE_{1,5}$ mode in LPG1 was similar to that of the $HE_{1,4}$ mode in LPG2 and their temperature sensitivities were opposite in sign. This property makes it possible to discriminate between the temperature and strain effects simultaneously [31].

Figure 4.10a shows the simple structure of the sensing probe based on dual LPGs for simultaneous measurement of strain and temperature. A cladding mode stripper between the two gratings is required to remove the interference pattern because the cladding modes coupled from the core mode by the first LPG can interfere with the core mode again in the second LPG. After fabricating LPG1, we tried to make LPG2 such that the resonance wavelength coincides with the main resonant wavelength of LPG1. To simply the sensing signal interrogation, peak separation and shifting of two LPGs with different temperature sensitivities and the same strain sensitivites were exploited. First of all, Two LPGs with positive and negative temperature sensitivities were fabricated to induce the peak separation with variations in temperature. Two LPGs, however, had similar strain sensitivity

so that resonant peak shift could be obtained with variations in strain. Since the temperature sensitivities of two LPGs are opposite in sign while the strain sensitivities are about the same, the resonant peak separation and shift should be induced as the external temperature and strain change, respectively. This allows unambiguous and simultaneous measurement of temperature and strain. The total loss including the splicing loss and the loss due to the mode mismatch was less than 0.1 dB. The overall length of the device is about 5 cm. Figure 4.10b shows the transmission characteristics of LPGs with the overlapped resonant wavelength. The circles show the resonant peaks of LPG2. In general, the core mode ($HE_{1,1}$) can be coupled to several cladding modes ($HE_{1,m}$) of LPGs [1] and the multi-resonant peaks appears in the transmission spectrum as seen in Fig. 4.10b (the dashed line). After fabricating LPG1, we measured the variation of the transmission spectra of the two gratings during the grating formation of LPG2. The resonant wavelength of LPG2 shifted to longer wavelength due to increase of the average index during the grating formation and finally overlapped with that of LPG1 as shown in Fig. 4.10b (the gray line). The resonant wavelength of $HE_{1,4}$ of LPG2 overlapped with that of $HE_{1,5}$ of LPG1, which has similar strain sensitivity and opposite temperature sensitivity. The overlapped wavelength makes it easier to measure the strain and temperature sensitivity with a single light source since we need to detect only one wavelength. All of the resonant peaks of two LPGs cannot be made to overlap consistently due to different photo-induced refractive index changes with the cladding mode order during the grating formation

Figure 4.11 shows the peak separation of the sensing probe as a function of temperature. The transmission characteristics of LPGs with the temperature change were shown in the inset. The peak separation was induced as the temperature increased because of the opposite temperature sensitivities of the two LPGs. Since the negative temperature sensitivity of LPG2 was larger in magnitude than the positive sensitivity of LPG1, the shift of the resonant peak to the left was larger than to the right. The temperature sensitivity of the sensing probe was

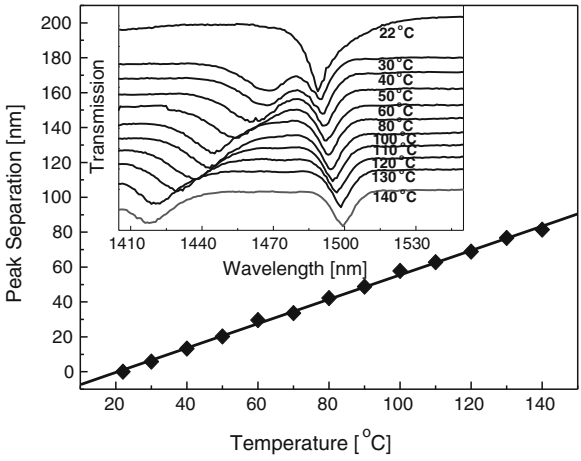

Fig. 4.11 Peak separation as a function of temperature. The transmission characteristics of the sensing probe with variations in temperature were shown in the inset [31]

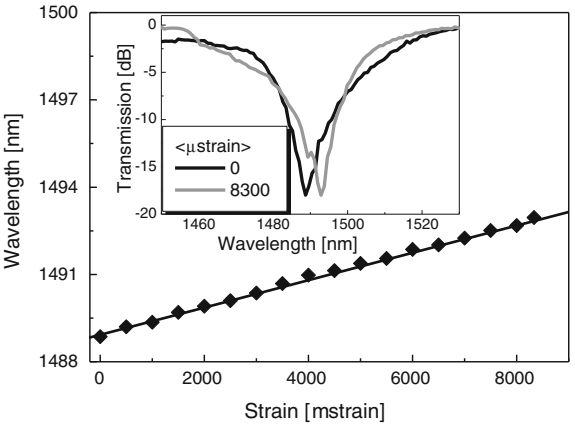

Fig. 4.12 Peak shift as a function of strain. Transmission spectra of the sensing probe with variations in strain were shown in the inset [31]

estimated as 0.69 nm/°C. Figure 4.12 shows the dependence of LPGs on the strain change and the transmission characteristics are shown in the inset. Since the two LPGs have similar strain sensitivity (∼0.46 nm/μstrain), the resonant wavelength shifted to the longer wavelength with the strain change. The measured strain sensitivity was 0.46 nm/μstrain.

4.4 Application III: Bio Sensors

Biosensors, including biomarker detection for medical diagnostics, and pathogen and toxin detection in food and water, have been attracting much attention. In general, since conventional biosensors have exploited a flouro-immunoassay method,.it is necessary to utilize the fluorescence labeling of the antigen or target DNA, which always requires additional reagents [32]. It means that the ordinary biosensors have many drawbacks, such as a high cost and the complicated and real-time detection configurations. To overcome these disadvantages, many methods have been applied to develop label-free detection biosensors [33, 34]. In particular, there has been much interest in fiber optic biosensors have been the promising techniques to realize high quality, label-free detection because of their various advantages, such as high sensitivity, fast detection speed, small size, variable and multiple detection of biosamples. A variety of biosensing techniques based on the fiber-optic surface plasmon resonance (SPR) phenomenon have been proposed [33, 35, 36]. In the case of the SPR biosensors, however, it is necessary to precisely design and fabricate the SPR biosensors because the SPR properties are highly sensitive to the metal contents, its thickness, and bio-molecules. Recently, biosensors based on fiber gratings have been widely investigated [37–41]. Most of fiber-grating-based biosensors have utilized long period gratings (LPGs) tuwith radiation mode coupling at resonance wavelengths that are very sensitive to the variation of the external medium [42]. To improve the sensitivity

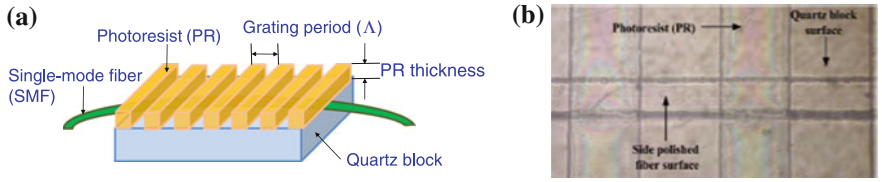

Fig. 4.13 **a** Scheme of the surface LPG. **b** Microscope image of the surface LPG [44]

of LPG-based biosensors, several methods, such as colloidal gold modified LPGs [39], LPGs with the etched cladding, [40], and LPGs with the nanostructured overlayer [41] have been proposed. However, these methods are disadvantageous because of the complicated and hazardous procedure, and the requirement of additional materials. A new, sensitive DNA biosensor based on a surface LPG inscribed on the surface of a side-polished fiber has been recently reported [43].

To fabricate a surface LPG, a single-mode fiber (SMF) was fixed by using an UV curable epoxy (NOA81) on a quartz block and ground down roughly on a brass plate by using an Al_2O_3 powder. The thickness of the cladding region was determined by measuring the transmission loss induced by the surface roughness [44]. Then, the roughly polised-SMF was polished again on a polyurethane plate by using a CeO_2 powder to reduce the surface roughness. After all polishing processes, the slurry on the flat surface should be removed by using an ultrasonic cleaning technique with de-ionized water and was dried at a temperature of $100^{O}C$ for 10 min. The photoresist (PR, Az4210) was coated on the surface of a D-shaped fiber by using a spin coater. Then, all samples were soft-baked in a thermal oven for 30 min at 90O C to remove some mixed solvent from the PR. In order to induce periodic surface gratings, the side-polished SMF with the PR coating was exposed to an UV lamp or an UV laser through a shadow long-period mask and developed by using a specific developer (Az400 k 1:3.5. Finally the periodic structure of the PR overlay on the surface of the side-polished fiber was periodically could be formed, which was a surface LPG. To stabilize the properties of the surface LPG, the post-baking process should be taken. Figures 4.13a and b show the scheme of the surface LPG and its microscope, respectively.

Since the refractive index of the PR-LPG overlay is higher than that of the core mode in the SMF, it couples the core mode to leaky modes excited by the surface PR-LPGs. When the effective index of the mth leaky mode is matched with the effective index (n_{eff}) of the core mode in the PCF, resonant coupling between the PCF and the surface PR-LPGs occurs. The resonant wavelength (λ_m) can be written as [45–47]:

$$\lambda_m = \frac{2d\sqrt{(n_g^2 - (n_{eff})^2)}}{m + \varphi}, \tag{4.67}$$

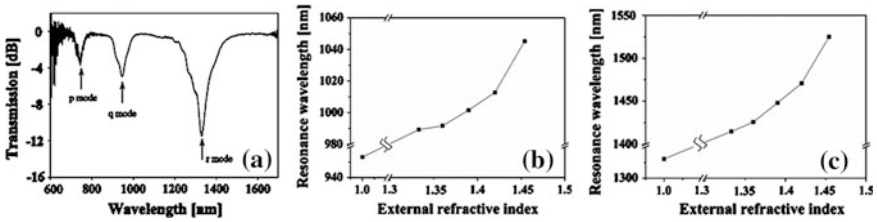

Fig. 4.14 (**a**) Transmission spectrum of the LPG, (**b**) resonance wavelengths of he q mode, and (**c**) r mode as functions of ambient indices [40]

where d and n_g are the thickness and the refractive index of the surface grating overlay, respectively. The phase change, φ, associated with external index change can be expressed by [45–47]

$$\varphi = tan^{-1}\xi \frac{(n_{eg}^2 - n_{ext}^2)^{\frac{1}{2}}}{(n_g^2 - n_{eg}^2)^{\frac{1}{2}}}, \tag{4.68}$$

where ξ is a polarization dependent constant. n_{ext} is an external refractive index. ξ can be determined by the polarization states [45–47]. It is clearly evident that external refractive index (n_{ext}) diminishes the amount of phase shift (φ), which contributes to the resonant wavelength shift to longer wavelengths [463-48].

Figure 4.14(a) shows the transmission spectrum of the surface LPG. The three different dips in the transmission spectrum indicate three different resonance wavelengths where a fundamental core mode couples to three leaky modes, p, q and r (named for convenience), in the surface LPG. Because the effective index of a high order leaky mode is smaller than a low order mode, the mode number of the r mode should be higher than that of the q mode and the resonant peak of the r mode should be appeared in a longer wavelength than other two modes. The biggest dip in Fig. 4.14a indicates that strong coupling occurred in the surface LPG between the fundamental core mode and higher mode order. Note that the resonance wavelengths, corresponding to the r and q modes, are changed with variations in the refractive indices of an external medium which are shown in Fig. 4.14b. As refractive index was increased, the resonant wavelengths shifted to a longer wavelength. When the refractive index was changed in a range from 1.333 to 1.454, the amount of resonance wavelength shifts for the q and r modes (as seen in Figs. 4.14b and c, respectively) were 84.4 nm and 110 nm towards a longer wavelength, respectively. The corresponding sensitivities were estimated to be 607.2 nm/RIU and 909.1 nm/RIU for the q and r modes, respectively. In this case, the resolutions of the biosensor were $1.6 \times 10 - 5$ and $1.1 \times 10 - 5$ RIU for the q and r modes, respectively. It is obvious that the r mode has higher sensitivity than the q mode because the higher order modes have higher sensitivity than the low order ones [2, 31].

Poly-L-lysine (PLL) has an extreme positive charge with NH_3^+ in the side chain and is frequently exploited for adsorbing biomolecules with negative charge like DNA (deoxynucleic acid) [48, 49]. A PLL solution (0.1 % W/V in water, the molecular weight = 150,000-300,000 g/mol, Sigma) was employed, which was commonly used in biology to treat glass slides. The surface LPG was initially cleaned by using a phosphate-buffered saline solution (NaH_2PO_4/Na_2HPO_4 pH 7.4, 150 mM NaCl) (PBS) before being modified with Poly-L-lysine. The PLL solution was dropped on the surface LPG to make a PLL layer for 160 min. at room temperature. The PLL layer functionalizes the surface LPG with an amino group at the free end, allowing a negatively charged DNA to be immobilized on the surface LPG. Then, the surface LPG is washed again by using a PBS buffer to remove excess PLL layers that were not immobilized on the surface LPG. The 1 μM probe of single-stranded DNA in the PBS buffer was then dropped on the surface of the PLL layer for 130 min. at room temperature. Then, the cleaning process was performed again. Finally, the 1 μM target single-stranded DNA in the PBS buffer was dropped on the surface of a probe ssDNA layer and after 65 min the sensor was washed by using a PBS buffer. About 100 μl of all biomolecules was added and removed using a micro-pipette. Figure 4.15 shows the molecular structure of the PLL, probe ssDNA and target ssDNA. The DNA sequences were (5'-CAG CGA GGT GAA AAC GAC AAA AGG GG-3') for the probe ssDNA and (5'-CCC CTT TTG TCG TTT TCA CCT CGC TG-3') for the target ssDNA.

The wavelength shift of the r mode in the surface LPG was measured, which was highly sensitive to external refractive index in a range from 1.333 to 1.454. As shown in Fig. 4.16 (a), the resonance wavelength shifted to a longer wavelength as the biomolecular layers was formed. When the PBS buffer was dropped on the surface LPG, the resonance wavelength was measured to e be 1411.69 nm. The immobilization of PLL on the surface LPG made the resonance wavelength shifted to 1413.52 nm. Then, when the probe ssDNA was immobilized on the PLL layer in the surface LPG, the shift of the resonance wavelength was measured to be

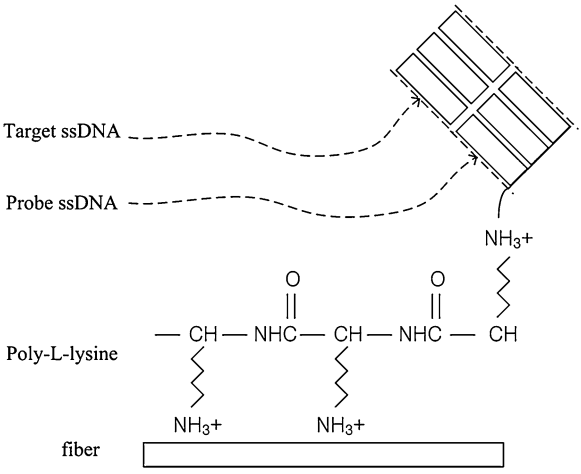

Fig. 4.15 Molecular structure of Poly-L-lysine, probe ssDNA and target ssDNA immobilized on the surface LPG [43]

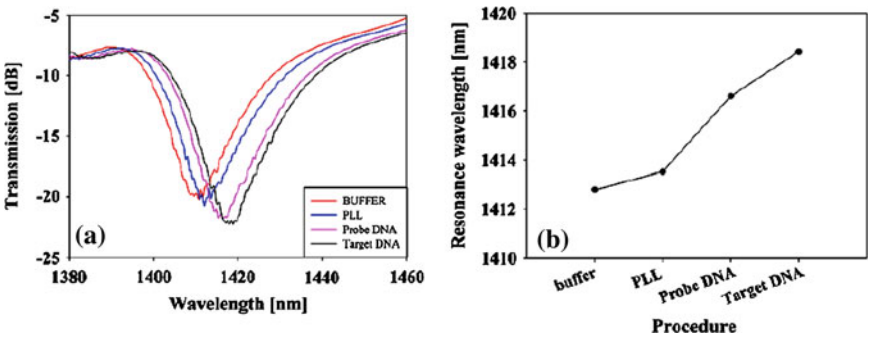

Fig. 4.16 (**a**) Transmission spectra and (**b**) resonant wavelength shifts of the surface LPG after sequential procedures of PBS buffer, PLL, probe ssDNA, and target ssDNA [43]

1416.61 nm. Finally, the hybridization with the complementary target ssDNA induced the a resonance wavelength shift of 1418.43 nm. The overall wavelength shift induced by the hybridization reaction was 1.82 nm, which is ~2.5 times higher than the previously reported biosensor based on a dual-peak LPG [49] under the same 1 μM target DNA concentration. It is evident that the surface LPG-based biosensor is highly sensitive to DNA hybridization in comparison with previously reported DNA fiber grating-based biosensors [38, 48]. The resonance wavelengths of the fiber grating-based DNA biosensor after each procedure are shown in Fig. 4.16 (b).

References

1. Vengsarkar AM, Lemaire PJ, Judkins JB, Bhatia V, Erdogan T, Sipe JE (1996) Long-period fiber gratings as band-rejection filters. J Lightwave Technol 14:58–64
2. Bhatia V, Campbell D, Claus RO, Vengsarkar AM (1996) Simultaneous strain and temperature measurement with long-period gratings. Opt Lett 21(5):336–338
3. Yariv A, Yeh P (1984) Optical Waves in Crystals. Wiley, New York, pp 177–185
4. Othonos A, Kalli K (1999) Fiber bragg gratings. Artech House, Boston, pp 189–221
5. Kogelnik H (1990) Theory of optical waveguides. In: Tamir T (ed) Guided-wave opto-eletctronics. Springer, New York
6. Eggleton BJ, Rogers JA, Westbrook PS, Strasser TA (1999) Electrically tunable power efficient dispersion compensating fiber Bragg grating. IEEE Photon Technol Lett 11(7):854–856
7. Kim J, Bae J, Han YG, Jeong JM, Kim SH, Lee SB (2004) Effectively Tunable Dispersion Compensation Based on Chirped Fiber Bragg Gratings without Central Wavelength Shift. IEEE Photon Technol Lett 16(3):849–851
8. Han YG, Lee SB (2005) Tunable dispersion compensator based on uniform fiber Bragg grating and its application to tunable pulse repetition-rate multiplication. Opt Express 13(23):9224–9229
9. Han YG, Lee JH (2007) Multiple elements photonic microwave true-time delay beamforming incorporating a tunable chirped fiber Bragg grating with symmetrical bending technique. Opt Lett 32(12):1704–1706

10. Choi ES, Na J, Ryu S, Mudhana G, Lee BH (2005) All-fiber variable optical delay line for applications in optical coherence tomography: feasibility study for a novel delay line. Opt Express 13(4):1334–1345
11. Han YG, Lee SB (2005) Tunable dispersion compensator based on uniform fiber Bragg grating and its application to tunable pulse repetition-rate multiplication. Opt Express 13(23):9224–9229
12. Akiyama M, Nishide K, Shima K, Wada A, Yamauchi R (1998) A novel long-period fiber grating using periodically released residual stress of pure-silica core fiber. Opt Fiber Conf Tech Dig 6:276–277
13. Hutsel MR, Gaylord TK (2012) Residual-stress relaxation and densification in CO2-laser-induced long-period fiber gratings. Appl Opt 51(25):6179–6187
14. Enomoto T, Shigehara M, Ishikawa S, Danzuka T, Kanamori H (1998) Long-period fiber grating in pure-silica-core fiber written by residual stress relaxation. Optical Fiber Conference Technical Digest 6:277–278
15. Lin CY, Wang LA (2001) Corrugated long-period fiber gratings as strain, torsion, and bending sensors. J Lightwave Technol 19(8):1159–1168
16. Yoon MS, Park SH, Han YG (2012) Simultaneous measurement of strain and temperature by using a micro-tapered fiber grating. J Lightwave Technol 30(8):1156–1160
17. Hwang IK, Yun SH, Kim BY (1999) Long-period fiber gratings based on periodic microbends. Opt Lett 24(18):1263–1265
18. Karpov VI, Grekov MV, Dianov EM, Golant KM, Vasiliev SA, Medvedkov OI, Khrapko RR (1998) Mode-field converters and long-period gratings fabricated by thermo-diffusion in nitrogen-doped silica-core fibers. Optical Fiber Conference Technical Digest 6:279–280
19. Dong L, Archambault JL, Reekie L, Russell PS, Payne DN (1995) Photoinduced absorption change in germanosilicate preforms: evidence for the color-center model of photosensitivity. Appl Opt 34(18):3436–3440
20. Fonjallaz PY, Limberger HG, Salathe RP, Cochet F, Leuenberger B (1995) Tension increase correlated to refractive-index change in fibers containing UV-written Bragg gratings. Opt Lett 20(11):1346–1348
21. Eom TJ, Kim SJ, Kimm TY, Park CS, Paek UC, Lee BH (2005) Realization of true-time-delay using cascaded long-period fiber gratings: theory and applications to the optical pulse multiplication and temporal encoder/decoder. J Lightwave Technol 23(2):597–608
22. Han YG, Lee BH, Han WT, Paek UC, Chung Y (2001) Controllable transmission characteristics of multi-channel long period fiber gratings. IEICE Trans Electron E84-C(3): 610–614
23. Khaliq S, James SW, Tatam RP (2001) Fiber-optic liquid-level sensor using a long-period grating. Opt Lett 26(16):1224–1226
24. Yun B, Chen N, Cui Y (2007) Highly Sensitive Liquid-Level Sensor Based on Etched Fiber Bragg Grating. IEEE Photon Technol Lett 19(21):1747–1749
25. Liu Y, Zhang L, Williams JAR, Bennion I (2000) Optical bend sensor Based on Measurement of Resonance Mode Splitting of Long-Period Fiber Grating. IEEE Photon Technol Lett 12:531–533
26. Dong X, Liu Y, Shao LY, Kang J, Zhao CL (2011) Temperature-independent fiber bending sensor based on a superimposed grating. IEEE Sensors J 11(11):3019–3022
27. James SW, Dockney ML, Tatam RP (1996) Simultaneous independent temperature and strain measurement using in-fibre Bragg Grating Sensors. Electron Lett 32:1133–1134
28. Guo T, Qiao S, Jia Z, Zhao Q, Dong X (2006) Simultaneous measurement of temperature and pressure by a single fiber Bragg grating with a broadened reflection spectrum. Appl Opt 45(13):2935–2939
29. Dong X, Liu Y, Liu Z, Dong X (2001) Simultaneous displacement and temperature measurement with cantilever-based fiber Bragg grating sensor. Opt Commun 192:213–217
30. Han YG, Dong X, Lee JH, Lee SB (2006) Simultaneous measurement of bending and temperature based on a single sampled chirped fiber Bragg grating embedded on a flexible cantilever beam. Opt Lett 31(19):2839–2841

31. Han YG, Lee SB, Kim CS, Jin U, Kang UC. Paek, and Chung Y (2003) Simultaneous measurement of temperature and strain using dual long-period fiber gratings with controlled temperature and strain sensitivity.Opt Express 11(5): 476–481
32. Charles PT, Vora GJ, Andreadis JD, Fortney AJ, Meador CE, Dulcey CS, Stenger DA (2003) Fabrication and surface characterization of DNA microarrays using amine- and thiol-terminated oligonucleotide probes. Langmuir 19:1586–1591
33. Homola J, Yee SS, Gauglitz G (1999) Surface plasmon resonance sensors: review. Sen Actuators B 54:3–15
34. Chinowskya TM, Quinn JG, Bartholomew DU, Kaiser R, Elkind JL (2003) Performance of the Spreeta 2000 integrated surface plasmon resonance affinity sensor. Sens Actuators B 91:266–274
35. Mehrvar M, Bis C, Scharer JM, Moo-Young M, Luong JH (2000) Fiber optic biosensors-trends and advances. Anal Sci 16:677–692
36. Masson JF, Barnhart M, Battaglia TM, Morris GE, Nieman RA, Young PJ, Lorson CL, Booksh KS (2004) Monitoring of recombinant survival motor neuron protein using fiber-optic surface plasmon resonance. Analyst 129:855–859
37. Maguis S, Laffont G, Ferdinand P, Carbonnier B, Kham K, Mekhalif T, Millot M (2008) Biofunctionalized tilted fiber Bragg gratings for label-free immunosensing. Opt Express 16(23):19049–19062
38. Chryssis AN, Saini SS, Lee SM, Yi H, Bentley WE, Dagenais M (2005) Detecting hybridization of DNA by highly sensitive evanescent field etched core fiber Bragg grating sensors. IEEE J Sel Top Quant Electron 11(4):864–872
39. Tang JL, Cheng SF, Hsu WT, Chiang TY, Chau LK (2006) Fiber optic biochemical sensing with a colloidal gold modified long period fiber grating. Sens Actuators B 119:105–109
40. Yang J, Sandhu P, Liang W, Xu C, Li Y (2007) Label free fiber optic biosensors with enhanced sensitivity. IEEE J Sel Top Quant Electron. 13(6):1691–1696
41. Wei X, Wei T, Xiao H, Lin YS (2008) Nano structured Pd-long period fiber gratings integrated optical sensor for hydrogen detection. Sens Actuators B 134:687–693
42. Lee KS, Erdogan T (2000) Fiber mode coupling in transmissive and reflective tilted fiber gratings. Appl Opt 39(9):1394–1404
43. Jang HS, Park KN, Kim JP, Sim SJ, Kwon OJ, Han YG, Lee KS (2009) DNA biosensor based on a long-period grating formed on the side-polished fiber surface. Opt Express 17(5): 3855–3860
44. Kwon OJ, Kim HJ, Han YG (2010) Dependence of the transmission characteristics of versatile D-shaped fibers on temperature and ambient index change for different input polarization states. J Korean Phys Soc 56(4):1274–1277
45. Kim HJ, Jun NR, Han YG (2012) Optical characteristics of a hybrid fiber grating based on surface long-period grating incorporating a fiber Bragg grating. J Korean Phys Soc 61(9):1353–1357
46. Kim HJ, Kwon OJ, Lee SB, Han YG (2012) Polarization-dependent refractometer for discrimination of ambient refractive index and temperature. Opt Lett 37(11):1802–1804
47. Kim HJ, Kwon OJ, Lee SB, Han YG (2011) Measurement of temperature and refractive index based on surface long-period gratings deposited onto a D-shaped photonic crystal fiber. Appl Phys B: Lasers Opt 102:81–85
48. Iadicicco A, Cusano A, Cutolo A, Bernini R, Giordano M (2004) Thinned fiber Bragg gratings as high sensitivity refractive index sensor. IEEE Photon Tech Lett 16(4):1149–1151
49. Sawant PD, Nicolau DV (2006) Hierarchy of DNA immobilization and hybridization on poly-L-lysine:an atomic force microscopy study. Smart Mater Struct 15:S99–S103